

Image Quality of the *Helioseismic and Magnetic Imager* (HMI) Onboard the *Solar Dynamics Observatory* (SDO)

R. Wachter · J. Schou · M.C. Rabello-Soares ·
J.W. Miles · T.L. Duvall Jr. · R.I. Bush

Received: 16 March 2010 / Accepted: 4 January 2011 / Published online: 10 February 2011
© The Author(s) 2011. This article is published with open access at Springerlink.com

Abstract We describe the imaging quality of the *Helioseismic and Magnetic Imager* (HMI) onboard the *Solar Dynamics Observatory* (SDO) as measured during the ground calibration of the instrument. We describe the calibration techniques and report our results for the final configuration of HMI. We present the distortion, modulation transfer function, stray light, image shifts introduced by moving parts of the instrument, best focus, field curvature, and the relative alignment of the two cameras. We investigate the gain and linearity of the cameras, and present the measured flat field.

Keywords Helioseismology, observations · Instrumental effects · Solar Dynamics Observatory

1. Introduction

The *Helioseismic and Magnetic Imager* (HMI) is a 14-cm aperture imaging solar instrument with an effective focal ratio of 37.4. It is built to operate in essentially monochromatic light at 6173 Å. The spectral filters are realized by the front window, a wide-band blocker filter, a tunable five-element Lyot filter, and two Michelson interferometers. The images are stabilized against spacecraft jitter by an Image Stabilization System (ISS) and recorded by

The Solar Dynamics Observatory
Guest Editors: W. Dean Pesnell, Phillip C. Chamberlin, and Barbara J. Thompson

R. Wachter (✉) · J. Schou · M.C. Rabello-Soares · R.I. Bush
Stanford University, Stanford, CA 94305, USA
e-mail: richard@sun.stanford.edu

J.W. Miles
Lockheed Martin Advanced Technology Center, Palo Alto, CA 94304, USA

J.W. Miles
SOFIA-USRA, NASA Ames Research Center MS N211-3, Moffett Field, CA 94035, USA

T.L. Duvall Jr.
Solar Physics Laboratory, NASA/Goddard Space Flight Center, Greenbelt, MD 20771, USA

two cameras, both equipped with a 4096^2 pixel CCD. Two legs at the back end of the HMI instrument allow a tilt of the optical axis to correct for long-term alignment drift of HMI versus the *Solar Dynamics Observatory* (SDO) satellite. Focus adjustment is achieved by placing a pair of fused-silica plane-parallel plates into the optical path. Two focus wheels with five openings, each with three plates of varying thickness, an open position, and a lens, which is used to image the aperture for calibration purposes, provide 16 discrete focus positions. For a detailed description of the optical design of the instrument, see Schou *et al.* (2011).

The optical calibration of the instrument aims at optimizing and characterizing the instrument in a way that allows us to calculate observables from the raw data (filtergrams) which are free from avoidable instrumental artifacts. The observables, the most important being magnetic fields and Doppler velocities, are fed into a data processing pipeline that resolves the surface and subsurface structure of the Sun (Couvidat *et al.*, 2010).

The instrumental effects that can be corrected through image processing must be known as accurately as possible, whereas the instrumental influences that cannot be corrected must be sufficiently small to meet the observable accuracy requirements. The instrumental artifacts that can be corrected in the observable calibration are the flat-field (detector and optical), the distortion, the relative alignment of the two cameras, and the residual image motion caused by movable parts in the instrument. Not easily correctable is a less-than-perfect modulation transfer function (MTF), caused by a variety of optical aberrations and leaking charges on the CCD, scattered light, and field curvature.

The calibration efforts therefore focus on:

- i) bringing the point spread function close to the optimum set by the diffraction limit and measuring the remaining optical aberrations. The stray light, which contributes to the tail of the point spread function, is measured separately.
- ii) measuring the distortion as accurately as possible.
- iii) setting the best focus in the middle of the available focal range for both cameras.
- iv) minimizing and characterizing field curvature and tilt.
- v) determining the misalignment of the cameras as accurately as possible.
- vi) minimizing the image motion introduced by the moving parts of the instrument, and obtaining consistent knowledge of the remaining movements.
- vii) measuring the nonlinearity of the camera response to light exposure, and verifying the saturation level.
- viii) measuring the gain of the detector amplifiers.
- ix) measuring the flat field on all scales, and monitoring its change in different environments.

We note that the above-mentioned characterizations can be repeated after launch, although certain tests must be performed in a different way. In some cases, more accurate calibration statistics are expected from the space measurements and will be made available. A detailed presentation of our results from the ground measurement and its later comparison with the in-flight measurements will show both the temporal drifts of the instrument and any effects of the launch, which will be instructional for future calibrations of imaging space instruments.

2. Calibration Setup

2.1. Instrument and Stimulus Telescope

All image-quality calibration measurements are performed with a stimulus telescope that provides a test beam with the correct Lagrange invariant. The target is mounted in the focal

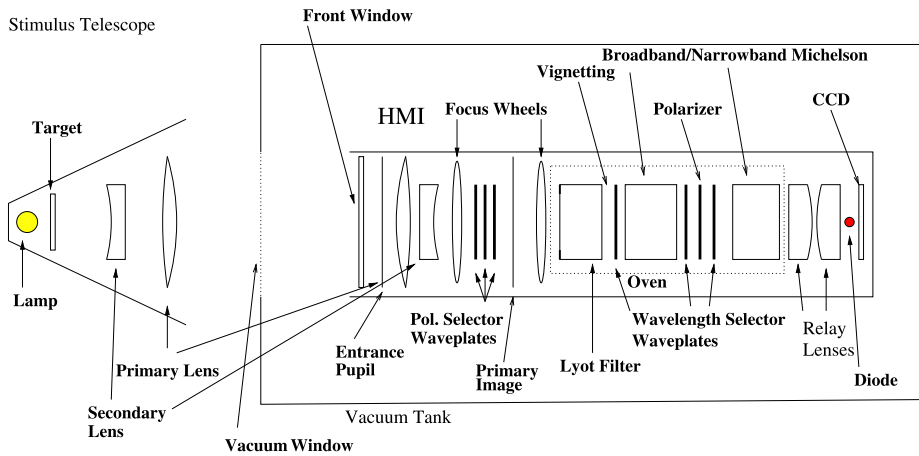


Figure 1 A schematic drawing of the calibration measurement setup showing only the elements most relevant for the image quality. Note also that the setup is not drawn to scale.

plane of the stimulus telescope with a lamp providing a source of white light. The optical axes of the stimulus telescope and the instrument are aligned (except for measurements where a controlled misalignment is required).

The system consisting of the stimulus telescope and the instrument was subject to thermal and vibrational perturbations in its environment. While the instrument has thermal control through various heaters and sensors at the instrument (with the spectral filters placed in the thermally controlled oven), the stimulus telescope has no such control. Instrument and stimulus telescope are stabilized against vibrational perturbations by use of a floating table. Blurring from turbulent air currents in the optical path and temperature variations are the major sources of noise in image-quality measurements.

Most of the time the instrument was subject to the same environment as the stimulus telescope (“in-air measurements”). However, the instrument was occasionally placed in a vacuum tank in order to test it at temperatures that resemble flight conditions. In particular, the dark current in the CCD detectors is drastically reduced, because the CCDs operate at much lower temperatures. In this setup, the collimated beam between the stimulus telescope and the instrument transits a glass window in the wall of the vacuum tank. This window is an additional uncontrolled element in the optical path of the system, introducing a temperature-dependent amount of optical power (and possible other aberrations) into the system.

Figure 1 shows a simplified layout drawing of the calibration setup including the optical elements of the instrument that are most important for the image quality. For a detailed optical prescription of the instrument, see Schou *et al.* (2011).

2.2. Test Facilities

The tests were carried out at the Lockheed Martin Advanced Technology Center (LMATC) in Palo Alto, CA before November 2007, at Goddard Space Flight Center (GSFC), Greenbelt, MD between November 2007 and July 2009, and at the Astrotech Facilities (ASO) in Titusville, FL until launch. The results from each series of measurements reflect the different thermal and vibrational perturbations of the environment. Also, the orientation of the stimulus telescope with respect to the instrument at LMATC was 90° different from the ori-

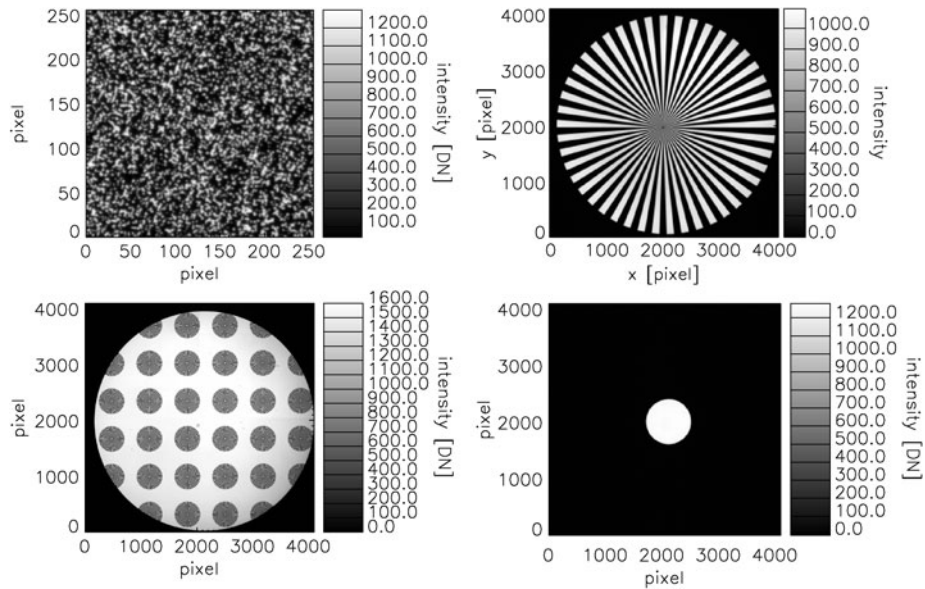


Figure 2 Focused instrumental images of different targets: the random dot target (upper left), the star target (upper right), the star array target (lower left), and the 5-mm field stop (lower right).

entation at the other two facilities. The instrument was put into the vacuum tank three times, but the instrument could be optically stimulated only for the first two times.

2.3. Targets

The most common stimulus telescope targets used for imaging are shown in Figure 2. They are:

- i)* The random dot target: A distribution of randomly placed dots of different diameters. The target provides a strong signal on all spatial scales. It is nonrepetitive at small scales, so that displacements can be measured uniquely and accurately. This is important for camera alignment and distortion measurements. The target is isotropic and has a translationally invariant power spectrum, which means that the relative MTF can be measured with the random dot target at any position and in any spatial direction, without any artifacts arising as a consequence of target properties. Best focus and the field curvature and tilt have been measured with the random-dot target.
- ii)* The star target: This target consists of a star with triangular rays of light and shadow. A star target is created to perform absolute measurements of the MTF. The response at each single spatial frequency is inferred from the different radial distances from the center. However, the different frequencies are measured at different field positions; the highest frequencies are measured at the center of the field, while the lowest frequencies are measured toward the edge of the field.
- iii)* The star-array target: Similar to the star target, but with multiple, smaller stars covering the optical field. While the very low spatial frequencies are not available, the star-array target examines the variation of the MTF across the field of view.
- iv)* The field stop target: A round field stop, which limits the field of view. We use field stops with diameter range from 5.0 mm to 27.4 mm, of which the largest is very close to

the edge of the field of view. Large field stops provide guidance about the alignment of the stimulus telescope and the instrument, while they introduce no signal for the HMI nominal field of view.

2.4. Light Sources

For most of the tests, we used an intensity-stabilized lamp, which feeds an optical-fiber bundle. The exit of the optical-fiber bundle is projected onto the aperture of the stimulus telescope.

Another light source is a Light Emitting Diode (LED), which sits behind the beam splitter in front of the cameras. The light is not transmitted through large parts of the instrument’s optics. In particular, it is not spectrally filtered, and the LED wavelength is different from the HMI target wavelength. With the LED, images can be taken even if it is technically not possible to feed light into the instrument. In this article, only the gain and linearity tests use data obtained with the LED.

3. MTF

3.1. Direct Measurement

The square-wave MTF can be directly measured by using a star target (see upper right panel of Figure 2). The response of the system to a single spatial frequency is derived from the image of the azimuthal square wave that corresponds to a given distance from the star center. The star is remapped in polar coordinates, and a sine wave is fitted for each radial distance.

For the incoherent imaging system under consideration, the amplitude $[A]$ at the spatial frequency λ is related to the MTF by

$$A(\lambda) = \text{MTF}(\lambda) \frac{2}{N} \left| \int_0^N dx \exp(2\pi i \lambda x) m(x) \right|, \tag{1}$$

where $m(x)$ is a cut through the remapped, normalized target image at a single frequency, and N is the dimension of the CCD in units of pixels. Representing an azimuthal cut through the star, the target object is given by

$$m(x) = 2\Theta(\sin(2\pi x \lambda)), \tag{2}$$

where $\Theta(x)$ is the Heaviside function.

The continuous integral is a sum of integrals over single pixels:

$$A(\lambda) = \text{MTF}(\lambda) \frac{4}{N} \left| \sum_{n=0}^{N/s-1} \sum_{m=ns}^{(n+\frac{1}{2})s-1} \int_{-\frac{1}{2}}^{\frac{1}{2}} dp \exp 2\pi i(m+p)\lambda \right|, \tag{3}$$

where N is the number of pixels, $s = 1/\lambda$ is the wavelength, and p is the lateral length of a pixel. The pixel integration can be performed explicitly, which leads to

$$A(\lambda) = \text{MTF}(\lambda) \frac{4 \sin(\pi \lambda)}{N \pi \lambda} \left| \sum_{n=0}^{N/s-1} \frac{2}{1 - \exp 2\pi i \lambda} \right|. \tag{4}$$

For $\lambda \ll 1$, we obtain

$$A(\lambda) = \text{MTF}(\lambda) \frac{4 \sin(\pi \lambda)}{\pi^2 \lambda}, \quad (5)$$

and hence

$$\text{MTF}(\lambda) = A(\lambda) \frac{\pi^2 \lambda}{4 \sin(\pi \lambda)}. \quad (6)$$

Although $\lambda \ll 1$ is not valid close to the Nyquist frequency, simulations show that expression (6) is valid to within 0.01 up to 80% of the Nyquist frequency where the MTF is measured.

The star-array target (see Figure 2) provides information about the large-scale spatial variation of the MTF.

The MTF can also be derived from the images of the random-dot target by dividing out the power spectrum of the target:

$$\text{MTF}(\lambda) = \frac{\int d\phi p(\lambda, \phi)}{\int d\phi t(\lambda, \phi)}, \quad (7)$$

where $p(\lambda, \phi)$ is the power spectrum of the image in polar coordinates, and $t(\lambda, \phi)$ is the power spectrum of the target in polar coordinates. The azimuthal average provides enough averaging at all relevant frequencies to make both numerator and denominator representative of their relative expectation values. Figure 3 shows estimates of the MTF derived from the star target and the random dot target.

Using the setup consisting of stimulus telescope and instrument, the wavefront error due to the stimulus telescope and instrument cannot be disentangled. To obtain the MTF of the instrument itself, the interferometric measurement of the aberrations in the stimulus telescope is subtracted from the measurement of the aberrations of the combined system (see Section 3.3).

We observed fluctuations in the measured MTF on small time scales, leading to a variation in the Strehl ratio of several percent. The magnitude of the fluctuations depends on the particular environment in which the measurements have been obtained. Both jitter and air currents are responsible for the random blurring on small time scales, while thermal degradations take effect on time scales of several minutes or longer. We conclude that air currents, rather than jitter, are the major source of noise, because the ISS removes most of the environmental jitter effectively. To take out the residual jitter, we placed the instrument and the stimulus telescope on a floating table, without noticeable improvements.

The test facilities at GSFC did not provide a stable room temperature, which caused the aberrations to vary with time, and, at the same time, degrade the MTF. In a thermally stable environment, the measured Strehl ratio is 0.74 ± 0.03 (see Figure 4). We define the Strehl ratio here as the peak intensity of the combined system of instrument and stimulus telescope divided by the peak intensity for the system as designed. Taking the point spread function as given by the diffraction limit of the instrument as a reference, the respective Strehl ratio of the full system (instrument + stimulus telescope) as designed is 0.980, whereas the Strehl ratio of the instrument as designed alone is 0.996. These numbers represent the height of the peak of the point spread function relative to the point spread function that represents the diffraction limit given by the aperture and the wavelength.

Strehl ratios above 0.80 have been measured. As we have no indications that the stimulus telescope is canceling out large parts of the wavefront errors of the instrument, we expect

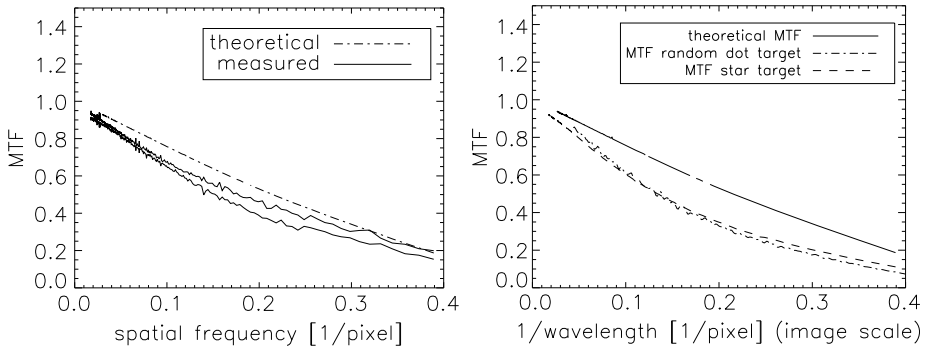


Figure 3 Left panel: The MTF measured with the star target. The theoretical curve represents the system of stimulus telescope and the instrument together. The two solid curves represent the MTF in the two perpendicular directions with the maximum and the minimum amplitude. Right panel: The azimuthally averaged MTF measured with the random dot target and the star target. The MTF can be inferred from the image of the random dot target by dividing out the known power spectrum of the target. Note that the left and right panels represent the MTF measured at different times. While we have not found any systematic changes, we observed random changes due to environmental perturbations.

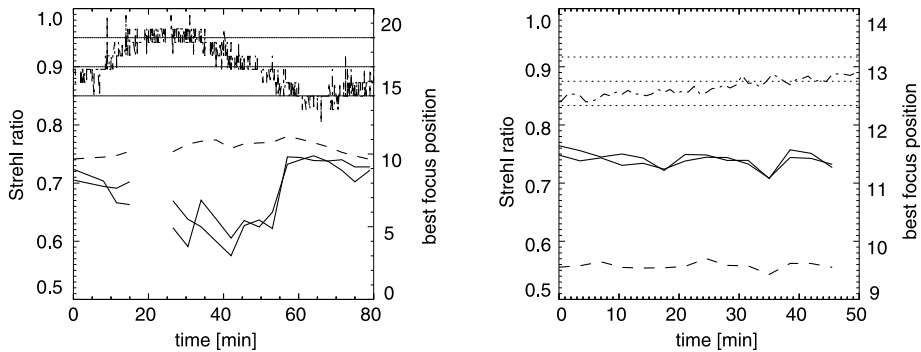


Figure 4 Left panel: Strehl ratio at best focus measured from a series of focus sweeps on a random-dot target in the test facilities of Goddard Space Flight Center in September 2008. The dashed curve gives the variation of the best focus. The upper curve shows the room temperature, with the three dotted lines representing 20.7, 20.8, and 20.9°C. Right panel: The same quantities as in the left panel, measured in the test facilities of Astrotech in August 2009. The horizontal lines represent 23.6, 23.7, and 23.8°C.

the Strehl ratio of the instrument to normally be at the upper end of all the measured values. Thermal perturbations and air currents introduce wavefront perturbations that generally degrade the MTF.

Our initial MTF measurements revealed a severe degradation of the MTF caused by the front window. We suspect that internal tensions caused by the layered front window design introduced large wavefront errors at the entrance pupil. As a remedy, the surface of the front window was polished to compensate for the internal wavefront error. Additionally, the known field-independent astigmatism of the instrument’s telescope is now compensated by the front window surface. The procedure resulted in a dramatic improvement of the MTF. Apart from the MTF variations caused by temperature gradients, we have not seen a degradation of the MTF over time.

Figure 5 Strehl ratio as a function of field position measured with the star-array target.

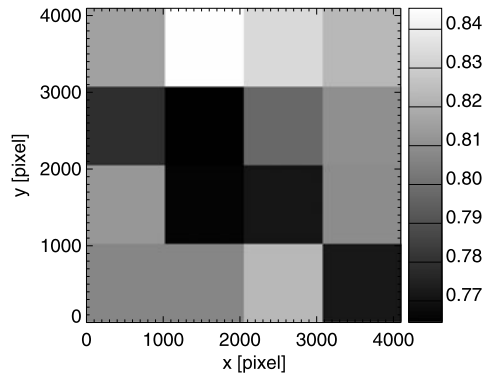


Figure 3 provides an estimate for the MTF of the combined system, comparing it to the function expected for a perfect instrument and stimulus telescope. This MTF represents a circular area of radius 400 pixels (about 200 arcsec) at the center of the image. As we have a clearly measurable amount of astigmatism in the system, we show the MTF in the two directions with maximum and minimum blur. For all other directions, the MTF will be in between these two lines.

3.2. Field Variations of MTF

For the variation of the MTF across the field, we need to assume that the target and the turbulent disturbances are homogeneous across the field. The star-array target shows an MTF that has a higher Strehl ratio off a diagonal from the upper left to the lower right corner of the CCD. Figure 5 shows the Strehl ratio measured for the central 16 stars (see Figure 2) of the star array target.

3.3. Phase Diversity Measurements

In order to further characterize the optical imperfections, we also performed a phase diversity analysis. To this end, focus sweeps of the random-dot target were used. As the deconvolved images are of no interest and as we were not successful in applying a traditional phase diversity algorithm, an alternative approach was taken.

To see how this method works, note that the cross spectrum of two images taken at different focus positions is the power spectrum of the true signal times the OTF at one position times the complex conjugate of the OTF at the other position. Like power spectra, but unlike Fourier transforms, cross spectra for multiple realizations may be averaged together to yield an estimate of the limit cross spectrum.

In the present case we averaged cross spectra from 16 128 pixel by 128 pixel patches near the center of the image. This was done for six pairs of focus position, using the best focus and the six adjacent focus positions. A model of the cross spectra was then fitted to the observed spectra while marginalizing over the power spectrum of the target.

This method was then tested with artificial data based on a ray trace and found to accurately reproduce the assumed aberrations.

The phase diversity analysis reveals several interesting results. The consistently most significant term is a spherical aberration of order -0.12 wave. The interferometry of the stimulus telescope indicates that it contributes about -0.02 wave and that the instrument thus has -0.10 wave, substantially more than the as-designed value of -0.01 wave.

The other terms are somewhat smaller. Unfortunately, it has proved difficult to correct them for the effects of the stimulus telescope, which was only measured on one occasion. The values we obtained from measurements at different test facilities were not consistent in all cases. A possible reason for this is that the stimulus telescope is not stable in time, because the mounts are not stress free.

We have also attempted to determine the Strehl values for the combined system from the phase diversity numbers. We found that while the numbers generally agree in magnitude, their variation does not agree with the variation estimated directly from the images. The cause of this is unclear, but it may be related to nonuniformities in the stimulus-telescope illumination.

4. Scattered Light

The instrumental scattered light can lead to important systematic effects, most importantly in the umbrae of sunspots where the scattered light may be a significant fraction of the intensity (Bray and Loughhead, 1979). Properly characterized, scattered light can be deconvolved, as was done by Jefferies and Duvall (1991) and Toner, Jefferies, and Duvall (1997).

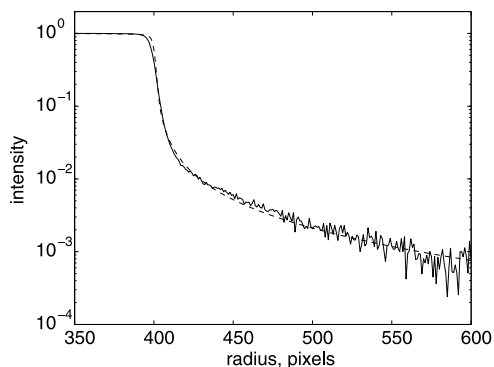
To characterize the scattered light in the HMI instrument, a field stop of radius 400 pixels is imaged onto the CCD through the optical system. Ideally, this would appear in intensity as a disk convolved with the diffraction limit MTF. In Figure 6, the azimuthally averaged intensity is shown out to about 200 pixels from the edge, where it falls to 10^{-3} of the disk intensity. Overplotted on the data is the result of a model calculation.

We would like to develop the point spread function (PSF) of this instrument to include the scattering that leads to the extended tail in Figure 6. A simple empirical model of the PSF, with parameters describing a narrow core and an extended tail of the PSF, is given by Pierce and Slaughter (1977):

$$A(r) = (1 - \epsilon)e^{-(r/w)^2} + \frac{\epsilon}{1 + (r/W)^\kappa}, \quad (8)$$

where r is the radial distance, ϵ determines the relative sizes of the two parts, w is the $1/e$ width of the central Gaussian core, W is the half-width at half-maximum width of the extended tail, and κ determines how fast the extended tail drops off. To determine a set of parameters that fits the observations, a disk of radius 400 pixels (which is a model for the field stop) is convolved with the model PSF. The parameters $\epsilon = 0.1$, $\kappa = 3.0$, $w = 1.8$, and

Figure 6 The azimuthal average intensity versus radial distance from the center of the field stop.



$W = 3.0$ provide the best fit. The result is plotted together with the data in Figure 6. While the overall fit is good, the small deviation near the edge can be attributed to the simplified representation of the core function as a Gaussian. However, here we are mainly concerned with the extended tail, as we believe the stray light to result from high-angle scatter in the optical elements of the instrument.

Using this function, the scattered light can be removed by deconvolution in regions where it is important, such as sunspot umbrae.

5. Distortion

5.1. Distortion Measurement

To measure the distortion, the random-dot target was mounted in the stimulus telescope. Images were taken at various alignment leg positions. Small areas of the images (256×256 pixels), corresponding to the same location on the target, but different positions in the optical field, were cross-correlated. The estimated shift between them corresponds to the difference in the leg position of the images plus the difference in the amount of distortion of the regions. This method of measuring distortion has the advantage that it does not depend on knowledge of the absolute properties of the stimulus telescope and the target. The distortion as a function of field position is expanded in Zernike polynomials, defined as

$$Z_n^m(\rho, \phi) = N_n^m R_n^m(\rho) \cos(m\phi) \quad \text{for } m \geq 0, \quad (9)$$

$$Z_n^m(\rho, \phi) = -N_n^m R_n^m(\rho) \sin(m\phi) \quad \text{for } m < 0, \quad (10)$$

where ϕ is the azimuthal angle and the ρ is the normalized radial distance ($0 \leq \rho \leq 1$). N_n^m is the normalization factor. R_n^m is the radial polynomial where $n - m$ must be even.

We used Zernike polynomials up to the 23rd order; *i.e.* we fitted the coefficients $a(n, m)$ in the expression

$$\mathbf{D}^f(\rho, \phi) = \sum_{n=2}^{23} \sum_{m=-n}^n \mathbf{a}(n, m) Z_n^m \quad (11)$$

to the observed data. No significant improvement was found by including higher-order Zernike polynomials.

Zernike polynomials were chosen because they are orthonormal over a unit disk. In our model, the terms with $n = \{0, 1\}$ are omitted, forcing the value at the CCD center to zero, as well as the terms describing the image scale, the roll, and the ellipticity. Those terms are unconstrained by the offset method to determine the distortion. Our model was fitted to the observed shifts using a nonlinear least-square fit. The Zernike coefficients are estimated together with the errors in the nominal leg positions. This way, the obtained distortion does not depend on an exact knowledge of the displacement caused by offsetting the alignment legs. Several sets of images were taken from June 2007 to August 2009. We fitted the distortion for each of 29 sets.

5.2. Distortion Results

To get a best estimate of the distortion, the fitted distortion at a given focus position and camera was averaged over all image sets. This best estimate of the distortion is shown in

Figure 7 Estimated distortion near best focus (focus position nine) for the front camera.

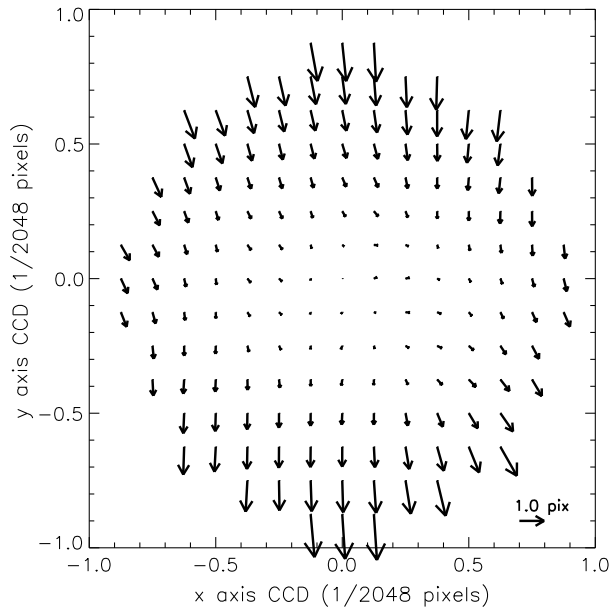


Figure 7 for the front camera near nominal best focus (focus nine). The distortion is smaller than two pixels at any field position.

We measure the magnitude of the residuals by

$$R_j = \sqrt{\sum_{\mathbf{r}} |\mathbf{D}_j(\mathbf{r}) - \mathbf{D}_j^f(\mathbf{r})|^2 / (2N_r)}, \tag{12}$$

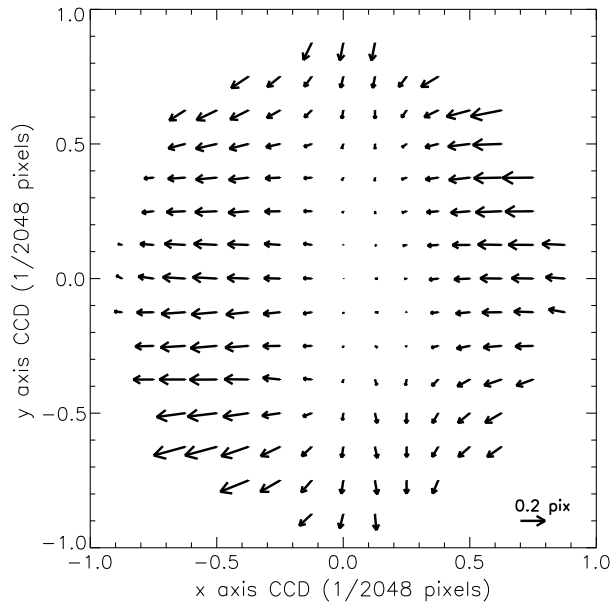
where \mathbf{D}_j is the distortion vector measured at a particular set, and \mathbf{D}_j^f is the best fit for each of these measurements. We average over all N_r points in the spatial grid. This number represents the error of individual measurements. The mean over R_j and its standard deviation are 0.043 ± 0.005 pixel for the front camera and 0.044 ± 0.005 pixel for the side camera near best focus. This number increases away from best focus, because shifts obtained from cross correlations are less accurate for blurred images.

We compare this number with the deviation from the mean of all measurements:

$$S_j = \sqrt{\sum_{\mathbf{r}} |\mathbf{D}_j^f(\mathbf{r}) - \overline{\mathbf{D}^f(\mathbf{r})}|^2 / (2N_r)}. \tag{13}$$

The mean and the standard deviation of S_n are 0.057 ± 0.027 pixel for the front camera and 0.050 ± 0.026 pixel for the side camera. This number increases to 0.10 pixel when the image is out of focus. This means that the changes seen over time are not significant beyond the two σ level. A closer look at individual sets suggests that the variation increases slightly when the temperature of the environment is unstable. This indicates that, within the accuracy of our measurements, the distortion is only weakly sensitive to the different thermal environments in which the measurements have been taken, and has remained constant throughout the integration of the instrument into the satellite.

Figure 8 Difference between the distortion of the front camera and the side camera for focus position nine. The difference has been obtained as an average from all available sets of measurements.



5.3. Variation of the Distortion with Camera

The mean difference between the distortion in the two cameras was calculated by averaging the difference between the fitted distortion for each camera over all sets at a given focus position. Figure 8 shows the mean difference between the two cameras at focus position nine (which is the nominal best focus of the instrument). The difference is everywhere smaller than 0.28 pixel. The differences in the distortion in the horizontal direction are statistically significant ($\approx 10\sigma$) and larger than in the vertical direction, which are barely significant ($\approx 2\sigma$), where σ is a standard deviation derived from the difference between the two cameras for different data sets. The additional distortion is caused by an element behind the beam splitter that separates the optical path of the two cameras, or by the CCD itself. We suspect the folding mirror to be responsible for the observed difference in the cameras.

5.4. On Orbit Rolls and Offsets

The image scale, ellipticity, and roll angle will be measured in space by looking at the size and shape of the solar disk, and by determining the relative position coordinates of the solar and lunar disk during lunar transits.

The elliptical distortion can be distinguished from anisotropies in the spectral solar image by rolling the spacecraft around the spacecraft–Sun axis and measuring the changing shape of the solar limb.

By a combination of rolls and offsets, it is also possible to determine further terms in the distortion by tracking the limb and supergranulation, as demonstrated with the Michelson Doppler Imager (MDI) (Korzennik, Rabello-Soares, and Schou, 2004). The plan is to do such calibrations on a regular but infrequent basis.

6. Focus and Camera Alignment

To determine the best focus position, we take an image of the random-dot target at all available focus positions (“focus sweep”) and look for the maximum spatial power at intermediate frequencies, where the power depends most strongly on focus (between 13% and 28% of the pixel Nyquist frequency). Fitting a quadratic function to the average power as a function of focus position allows us to determine the best focus in fractions of focus steps. The random blur introduced by air currents limits the accuracy of single measurements of the best focus to 0.1 focus step.

As the setup of the stimulus telescope tries to achieve a nearly collimated beam entering the instrument, focusing on the target is equivalent to focusing on the Sun. An air-to-vacuum corrector in front of the instrument corrects for the fact that there is air in the instrument. We aim at a best focus in the middle of the available focus from position one through sixteen. The best focus of the two cameras should not differ by more than 0.5 focus step. Table 1 (right columns) gives the focus of both cameras for different measurements. Focus position nine is just above the middle of the available focus range, and is the nominal best focus of the instrument. We tried to bring the best focus of the instrument slightly above the middle of the focus range, because the heaters at the front window are able to lower the best focus position, but not to raise it.

The measured focus of the instrument shows some variation. We know that a temperature gradient across the front window introduces refracting power. While the heaters at the rim holding the front window control the temperature at the edge, the center of the window is largely dominated by the air temperature. Therefore, a good control of the front window gradient is difficult to achieve in the absence of a strictly controlled room temperature. This is reflected in the fluctuating focus values. However, the focus difference between the front and side cameras are well within the tolerance limits, with a marginally higher focus (≈ 0.2 focus step) for the front camera.

Note that the best focus cannot be reliably measured when the instrument is in the vacuum tank, as the window of the vacuum tank introduced unknown refracting power to the system.

Some of the proposed observables frame lists require us to combine the raw images of both cameras. To do so, the coalignment of the cameras must be known accurately. The alignment of the cameras can be determined from simultaneous focus sweeps on both cameras by using cross-correlation techniques. We derived a relative lateral shift and a relative rotation for the images of the two cameras, and found the lateral shift to slightly drift over

Table 1 Relative lateral shift between the two cameras (x, y), the relative rotation (rot) in degrees, and the best focus position (range: 1–16) for the front and side cameras for different measurements during the calibration campaign.

Date	x	y	rot	Focus front	Focus side
18-Feb-2008	-6.6	5.5	0.082	10.9	10.9
14-Feb-2008	-6.4	5.7	0.081	9.7	9.4
30-Jan-2008	-6.2	5.3	0.082	8.2	8.2
03-Nov-2007	-6.1	4.3	0.079	10.4	10.3
02-Nov-2007	-6.2	4.3	0.080	9.9	9.7
28-Oct-2007	-6.7	3.5	0.080	8.8	8.7
14-Oct-2007	-4.5	4.5	0.082	9.1	9.1

time scales of several months. The relative shifts and rotations are given in Table 1. The observed long-term changes are most likely caused by the changing mechanical stresses on the instrument or the changing thermal environment. We are able to measure the shifts very accurately in space and to monitor them continuously.

7. Field Curvature

Field-curvature measurements use the same data sets as distortion measurements. Image offsets, using the alignment legs to vary the pointing, allow us to distinguish between the properties of the stimulus telescope and the instrument. The images in the front camera and the side camera were recorded alternately. Using the random-dot target, we measure the best focus as a function of field position, and fit the model:

$$f(x, y) = a_Hx + b_Hy + c_H(x^2 + y^2) + a_S(x - x_L) + b_S(y - y_L) + c_S((x - x_L)^2 + (y - y_L)^2) + d. \quad (14)$$

Here, x and y are coordinates of the HMI image and x_L and y_L are the image shifts introduced by offsetting the optical axis of the instrument using the alignment legs. x_L and y_L can be measured by cross-correlating the images of the random dot target. a_H and b_H measure the horizontal and vertical component of the HMI field tilt, and c_H measures the (quadratic) field curvature. a_S , b_S , and c_S measure the respective quantities for the stimulus telescope. Using all 13 or 25 leg positions, the coefficients $a_{H,S}$, $b_{H,S}$, $c_{H,S}$, d are overdetermined and can be obtained from a least-square fit. Note that the constant focus term $[d]$ does not separate between the stimulus telescope and the instrument.

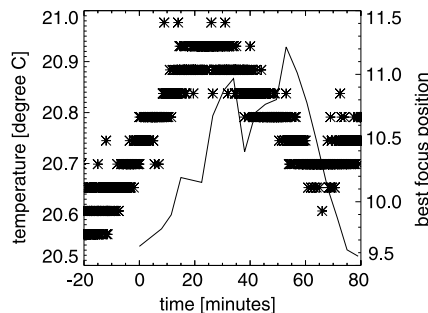
We found that while there is consistency in the inferred quadratic term, the linear-gradient term fluctuates wildly.

Field-curvature measurements at GSFC were performed in an unstable temperature environment, which leads to a changing of the focus with time. Figure 9 shows a measurement of the best focus together with a record of the outside temperature. It indicates that the focus position follows the temperature gradient with a time lag.

As the model described by Equation (14) assumes a focus independent of time, temporal variation of the focus led to spurious field tilts.

In order to understand the fluctuations of the measurements, we performed a series of 12 field curvature sequences with identical setup. Figure 10 shows the strong anti-correlation between the gradients measured for the stimulus telescope and the instrument.

Figure 9 The stars represent the measured air temperature during a continuous focus measurement, and the line shows the measured focus. The focus follows the temperature with a time lag of 18 minutes.



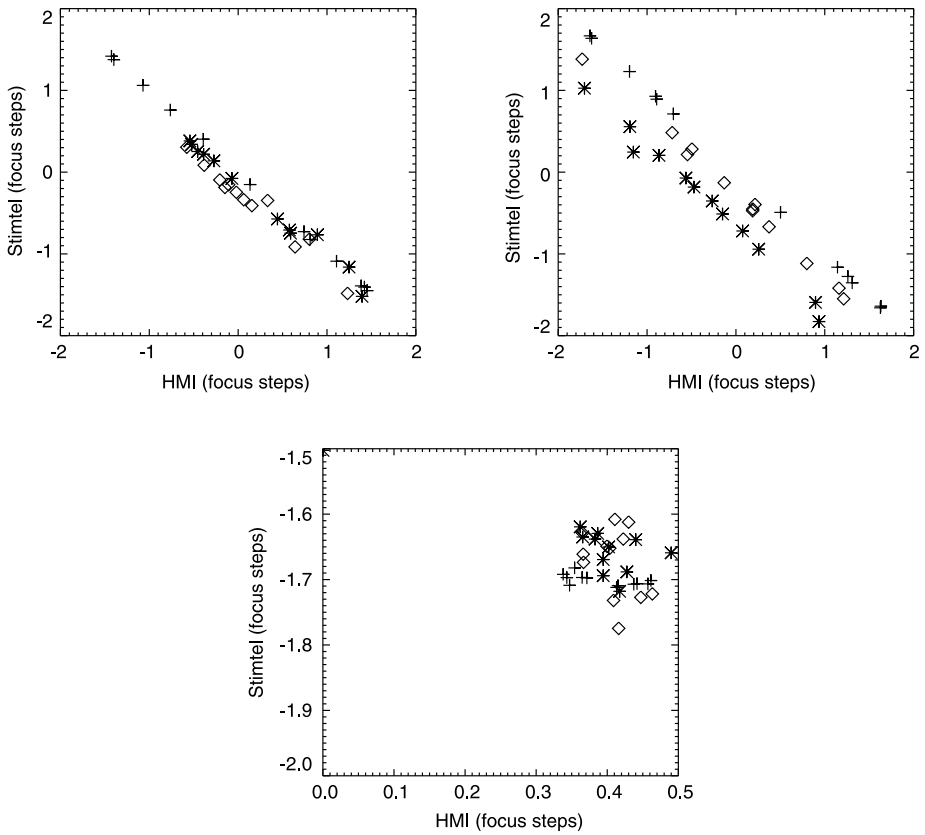


Figure 10 Horizontal (upper left) and vertical (upper right) field tilt as measured for the front camera (diamonds) and the side camera (stars), together with the result of the simulated measurements (crosses). The simulations enable us to explain the variations as an artifact caused by an unstable outside temperature. The lower panel shows the quadratic term, which has no strong sensitivity to the temperature drift.

We simulated a sinusoidal focus drift with a period of 2.2 hours, and an amplitude of 0.75 focus steps, and a random phase. These parameters represent observed focus drifts when we measured the focus continuously, showing that the major properties can be reproduced. For the field-tilt parameters, we see the characteristic, nonphysical anti-correlation of stimulus telescope parameters and instrument parameters. Still, the field-curvature parameters are not biased if the measurements are started at a random time, and therefore their average value provides an estimate for the actual tilt.

We observed that the coefficients for the front and side cameras are strongly correlated. This suggests that jitter or air currents, which act on the short time lag between the cameras and would destroy the correlation, play a minor role in the observed variation in the field tilt parameters. Table 2 gives the mean value and standard deviation of the 12 consecutive measurements.

Figure 11 shows all of the field-curvature measurements that we obtained at the different test facilities. While the temperature fluctuations at GSFC caused large fluctuations of the measured values, the environments at LMATC and ASO were more stable, which resulted in more consistent values.

Table 2 Field tilt and curvature for the front and side cameras. The numbers represent the focus change in units of nominal steps from edge to edge for the focus gradient, and the change from center to edge for the quadratic focus term. The numbers have been derived from a series of twelve field-curvature measurements in an unstable temperature environment at GSFC.

	Grad x	Grad y	Quadratic
Front cam. June 2008	0.01 ± 0.15	-0.13 ± 0.24	0.40 ± 0.01
Side cam. June 2008	0.09 ± 0.17	-0.45 ± 0.20	0.41 ± 0.01

We conclude that the side camera has a vertical gradient in the best focus position with the top of the field being half a focus step lower than the bottom. The gradient observed for the front camera is not significantly different from zero. This suggests that the plane of the side camera CCD slightly deviates from vertical to the optical axis. The field curvature increased initially, but later settled at a value of 0.4 focus step from center to edge.

8. Image Motion

There are several moving parts in the instrument that can potentially lead to image offsets. While they can be corrected before the observables are calculated, they must be known precisely, because any error will lead to crosstalk between the spatial domain and the wavelength domain. Both *a priori* knowledge of shifts introduced by particular waveplates and Sun-center coordinates obtained by fitting the solar limb in individual filtergrams provide information about the instrumental image motion.

There are six rotating waveplates and one rotating polarizer in the instrument. Three waveplates are used for the polarization selection, and three of the waveplates and the rotating polarizer are used to tune the Michelson interferometers and the tunable Lyot filter.

In the following, we call them POL1 ... POL3 (polarization selectors) and WL1 ... WL4 (wavelength selectors), in the order in which the light is passing through them (see Figure 1). All waveplates have been separately rotated by 360° in steps of 30° . We determine the relative image shifts by cross-correlating each image with a reference image. Figure 12 shows an example of the detected image motions.

The most striking feature is the vertical motion with an amplitude of about half a pixel which is produced by the two wavelength-selector wave plates WL2 and WL4, *i.e.*, the waveplates tuning the two Michelson interferometers. We do not fully understand the reason why this vertical motion does not result in a phase-shifted horizontal motion, as would be suggested by a geometric distortion or a mounting error of the waveplates. However, the shift has been consistently seen on the ground, and it will be measured in-flight.

We note that while we detected a solid image shift with the rotating waveplates, the distortion introduced by the waveplates is generally only a few hundredths of a pixel. Occasionally observed shifts up to 0.1 pixel are not reproducible, and therefore are most likely thermally introduced distortions.

Other moving parts of the instrument are the two focus wheels. Because some glass blocks are not perfectly mounted or show a wedge, they shift the image by several pixels. Figure 13 shows the offset as a function of the position of the focus wheels. Unlike the polarization and wavelength-selector waveplates, the focus wheels do not move during regular observations. We note that focus-sweep observations, which will be performed regularly in space to determine the best focus position and the MTF, must take into consideration the finite reaction time of the ISS to the image shifts introduced by the moving focus wheels.

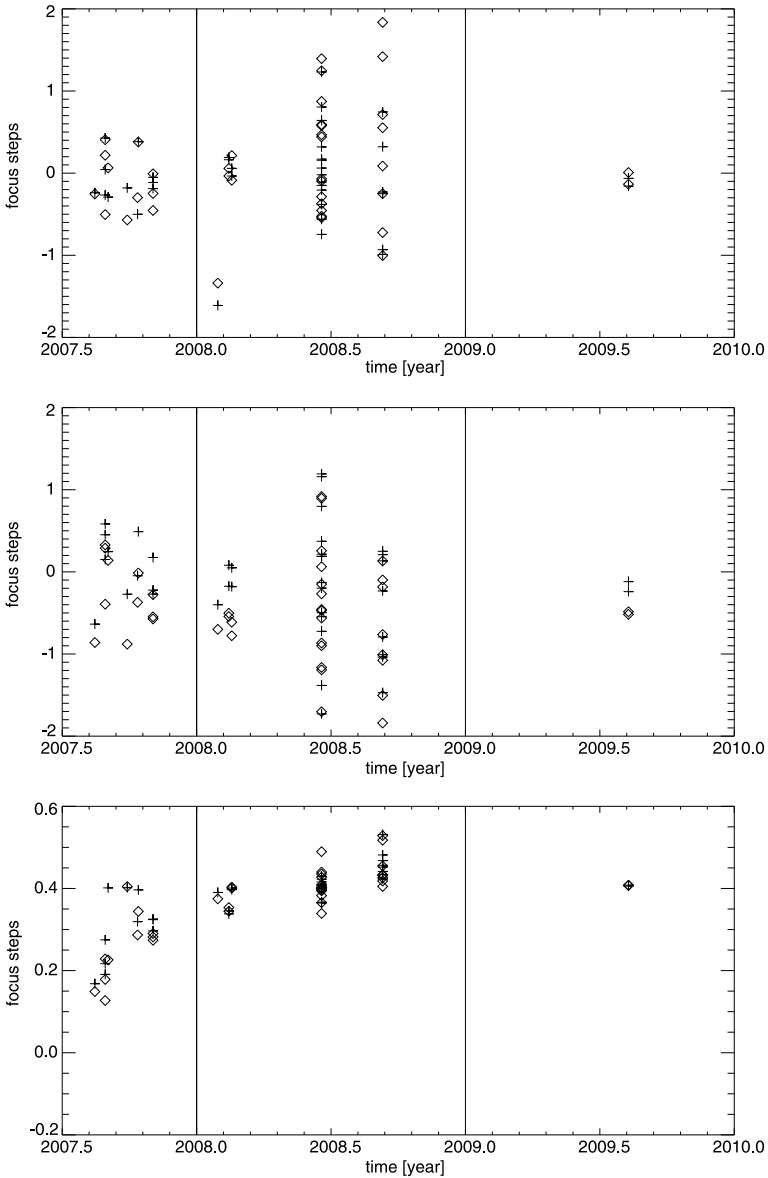


Figure 11 Measured value of the field tilt in horizontal (upper panel) and vertical (center panel) direction, and the quadratic field curvature (lower panel). The numbers represent the focus change in units of nominal focus steps from edge to edge for the focus gradient (left to right and bottom to top), and the change from center to edge for the quadratic focus term. The crosses show the data for the front camera, and the diamonds show the data for the side camera. The horizontal axis represents the time of the measurement. The left section represents the field values obtained at LMATC, the center section represents the values obtained at GSFC, and the right section represents the values obtained at ASO. At GSFC, temperature changes during the field-curvature sequence (which takes about one hour) introduce large fluctuations in the measured parameters, and only averages of a large number of measurements are meaningful. The values measured at LMATC and ASO suggest a field tilt of one-half focus step in the vertical direction for the side camera. The field curvature, which can be measured even in unstable temperature environments, has initially increased, but has stabilized later on.

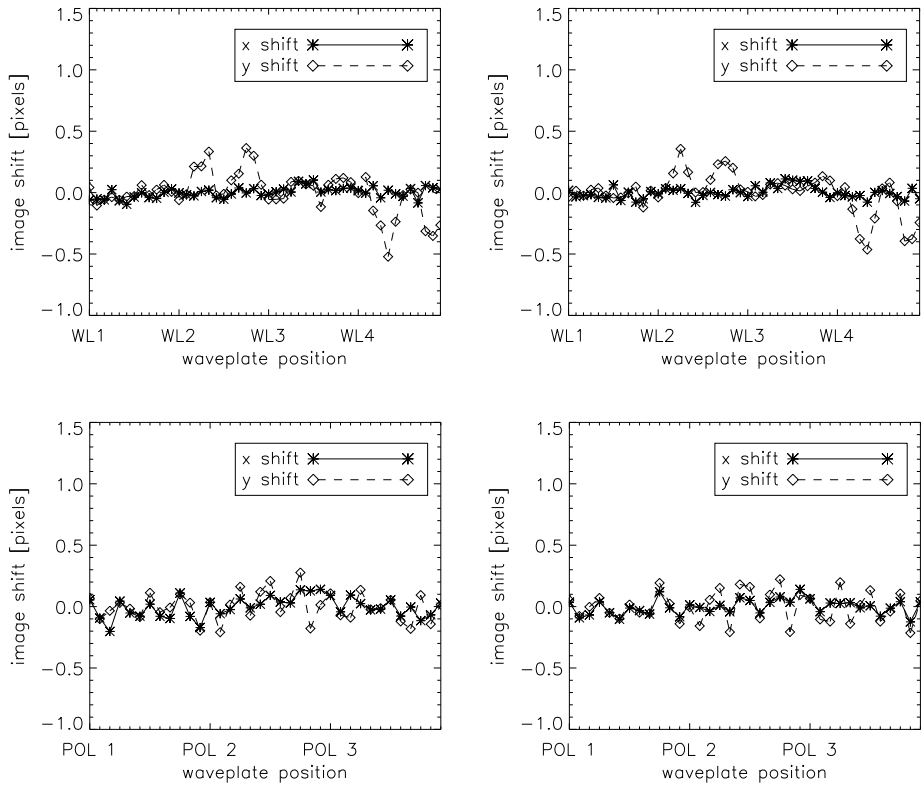
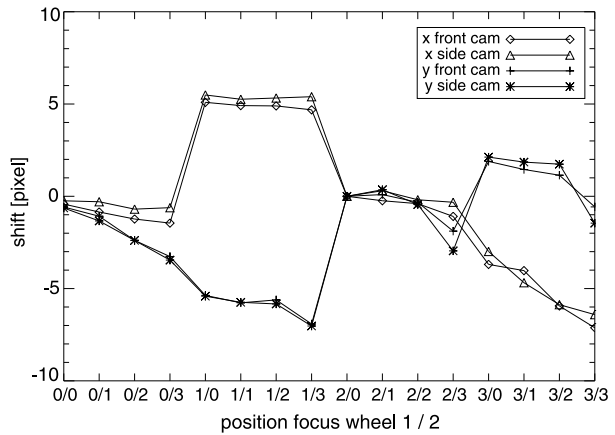


Figure 12 Image motion introduced by moving waveplates (upper panels) and polarizers (lower panels). The left panels show the front camera; the right panels show the side camera. The rotation of the indicated waveplate starts at the major tick marks, with a 30° increment for each minor tick mark.

Figure 13 The image shifts introduced by the focus blocks. The labels on the horizontal axis show the thickness of the first and second glass plates in the optical path. The thickness is a multiple of 3.4 mm for the first focus wheel and a multiple of 0.85 mm for the second focus wheel.



9. Flat Field

The flat field has been determined by the method presented by Kuhn, Lin, and Lorz (1991) and Toussaint, Harvey, and Toussaint (2003). Similar to the field curvature and distortion measurements, one can distinguish between the instrumental flat field and the inhomogeneous illumination of the stimulus telescope by tilting their optical axes with respect to each other. We used a 27.4-mm diameter field-stop target, which cuts off only the extreme edge of the field of view. It is large enough to not limit the field of view substantially, but it still gives guidance about the relative displacement of instrument and stimulus telescope. We note that, because the illumination varies only on large scales, the flat field does not depend critically on an extremely accurate knowledge of the image offsets.

The resulting flat field (see Figure 14) shows the different gains of the four quadrants of the CCD, as well as four slabs per quadrant, which are a result of the manufacturing process. This is not a property of the CCD surfaces, but of their respective amplifiers. The small-scale

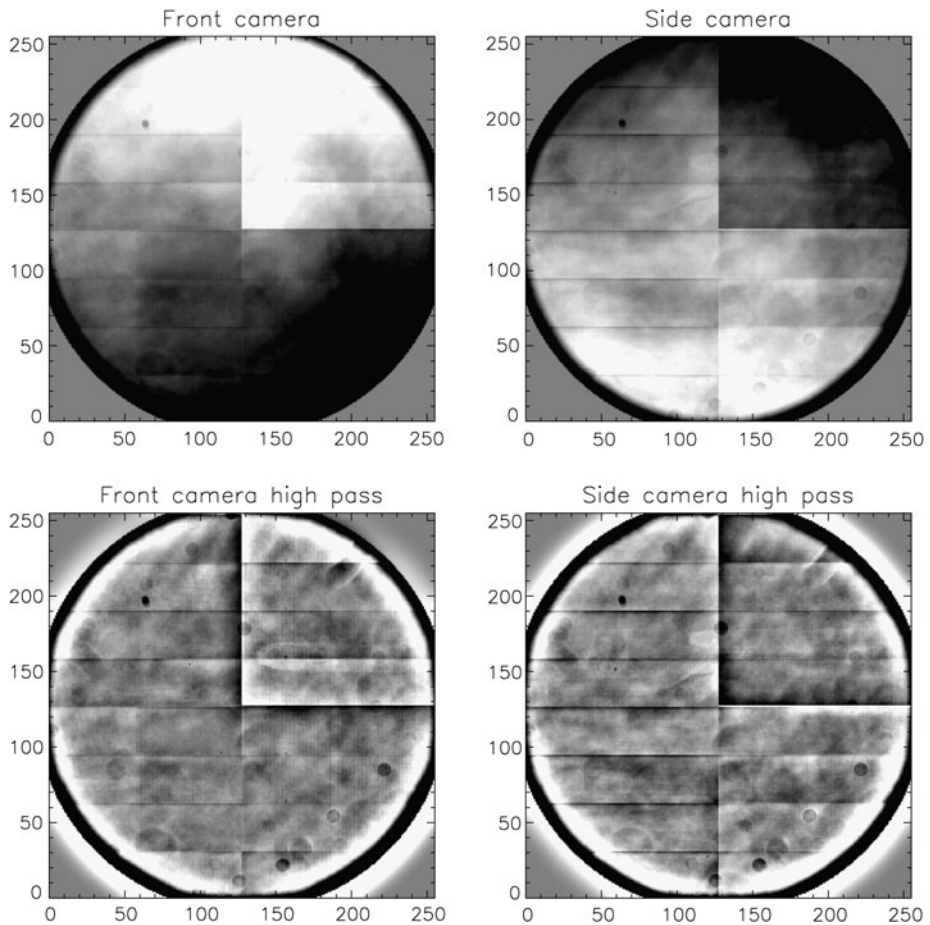


Figure 14 The panels show the flat field of the front and side cameras (left and right columns), with the high-pass-filtered version in the lower panels. In order to show the structure more clearly, the gray scale is saturated to $\pm 5\%$ for the flat field and $\pm 2\%$ for the high-pass-filtered version.

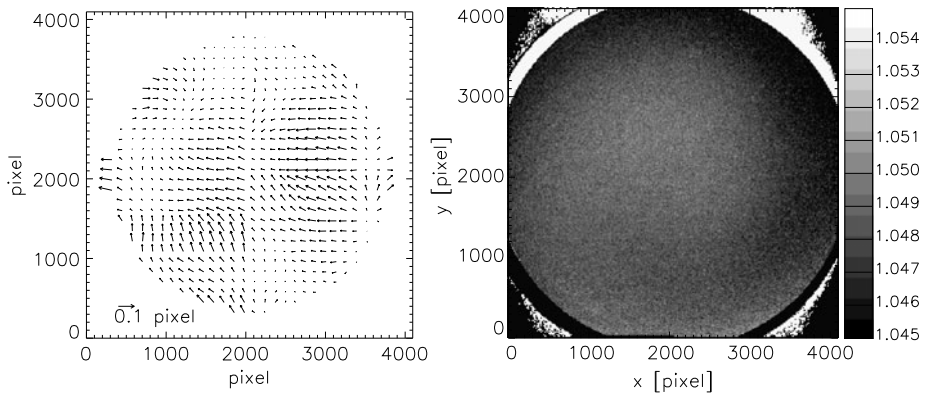


Figure 15 Left panel: Residual shifts between the images after removing a lateral shift, a rotation, and a fourth-order polynomial for the mutual distortion. The spatial structure is dominated by the 512×2048 pixel slabs of the CCD. Right panel: Averaged residuals from the offpoint flat field measurements. The residuals give an estimate of the error in the large-scale variation of the flat field. The average error inside the vignetting radius is 0.2%.

features of the flat field can be made visible by applying a high-pass filter to the flat field. The circular structures show out-of-focus dust specks that are part of the optical flat field. The optical flat field is largely identical for both cameras, whereas the CCD flat fields are independent.

The flat field falls off sharply near the edge of the field of view. This is a result of vignetting, caused by the opening at the back end of the Lyot filter being too small, which slightly obstructs the clear aperture of the instrument. The unvignetted part of the optical field is large enough to always fully contain a properly centered solar image. The observables should therefore be unaffected by the vignetting.

There is a larger dust speck on the side CCD camera obscuring an area of about twelve pixels (and several smaller ones on both cameras), reducing the intensity of several pixels below 50% of the normal value. The signal in these pixels is too low to be simply corrected by applying the flat field. The affected pixels need to be treated as missing pixels and spatially interpolated.

We also discovered a stable horizontal structure with a period of roughly 43 pixels. The structure shows different strengths for both CCDs and for the different quadrants, but no apparent temporal variation.

As a measure of the large-scale flat-field quality, we look at the magnitude of the residuals. Figure 15 (right panel) shows the average residuals from the offset images. The images have been rebinned to reduce the photon noise. The residuals are probably caused by slight variations in the aperture illumination, which are ignored in the flat-field derivation. The average residual inside the vignetting radius is 0.2%.

We noticed condensation on the CCD, which produced geometric patterns when the instrument was in the vacuum tank. Figure 16 shows how these patterns became stronger with time as long as the instrument was in the vacuum tank. Images taken with the internal LED at GSFC showed similar patterns. We expect the outgassing of the instrument at the beginning of the mission to be so thorough that condensation does not become a problem during normal operations. If contaminants should build up on the CCD, heaters can be switched on to clean up the CCD.

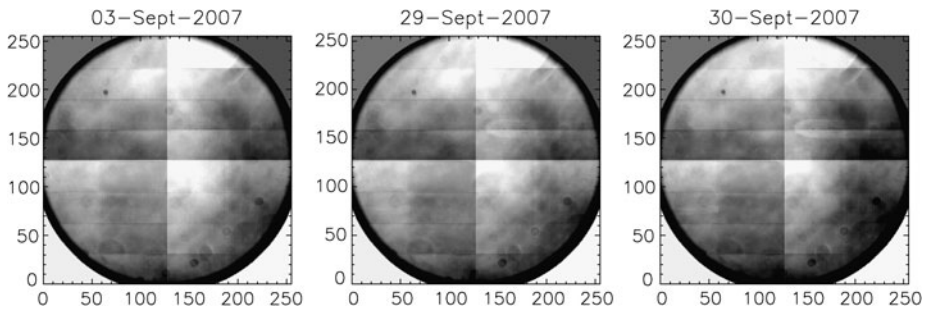


Figure 16 The three panels show the observed flat field in vacuum. The finger-like horizontal structure in the upper right quadrant becomes stronger with time. The gray scale is saturated with a range from 0.95 to 1.05 for better visibility of the structure. Also, the quadrants have been corrected for the different quadrant gains.

There are more stringent requirements on the small-scale flat field, because it is critical to the subpixel spatial interpolation of the filtergrams. The accuracy must be better than 0.1% at any given time. Besides the above-mentioned algorithm, small-scale flat fields can be obtained from any low-contrast image. The condensation patterns shown in Figure 16 lead to small-scale flat field changes over the entire CCD. Although the rate of the flat-field changes depends strongly on the particular thermal environment of the instrument, an order of magnitude estimate of the change may be derived from the fact that we saw a change of 0.2% in the area-average small-scale flat field within a period of five weeks in which the instrument was kept in the vacuum tank. A mechanism to monitor the small-scale flat field from regular filtergram observations at a temporal cadence of one day has been implemented to deal with any changes in the flat field (Wachter and Schou, 2009). This way, we expect to achieve a flat field knowledge of better than 0.1% at all times.

10. Gain and Linearity

10.1. Camera Gain

The gain of the amplifiers of the four quadrants of the CCD is determined by varying the exposure time and determining the slope of the variance *versus* the signal. A number of exposures from 0 to 16 seconds were taken with the LED while the instrument was in the vacuum tank. Figure 17 shows the average signal *versus* an estimate of the variance. The variance is estimated from a pixel-by-pixel difference of two identical images. We see a clear linear dependence before saturation is reached at around 12 000 DN. The variance drops after saturation, because the pixel stops collecting charge, and electric charge is leaking to neighboring pixels. Figure 18 shows the inverse gain as a function of CCD position for the front and the side camera. As expected, the gain is different for each quadrant. The variation within the quadrant is probably a residual effect from the very inhomogeneous illumination of the CCD, which results in a different weight across the intensity range. The average gain for each quadrant is given in Table 3.

10.2. Linearity

Another important aspect of the CCD and camera performance is the linearity of the amplifiers. The linearity can be derived from the same data set as the gain. The center four pixels

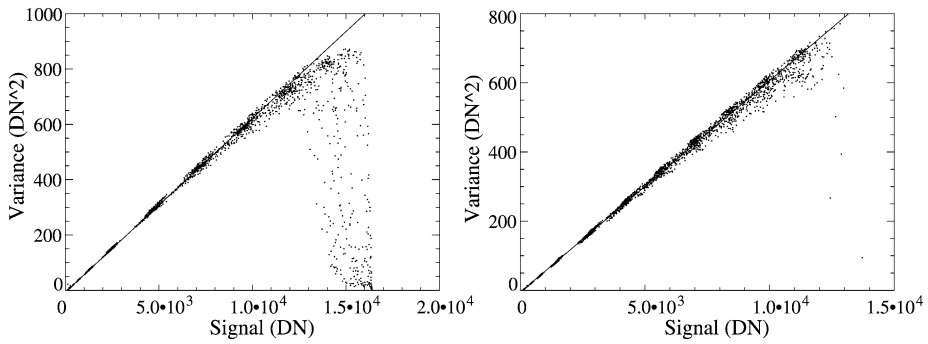


Figure 17 The variance as a function of signal intensity for front (left) and side (right) cameras. The slope of this curve in the linear range is the gain of the camera amplifiers.

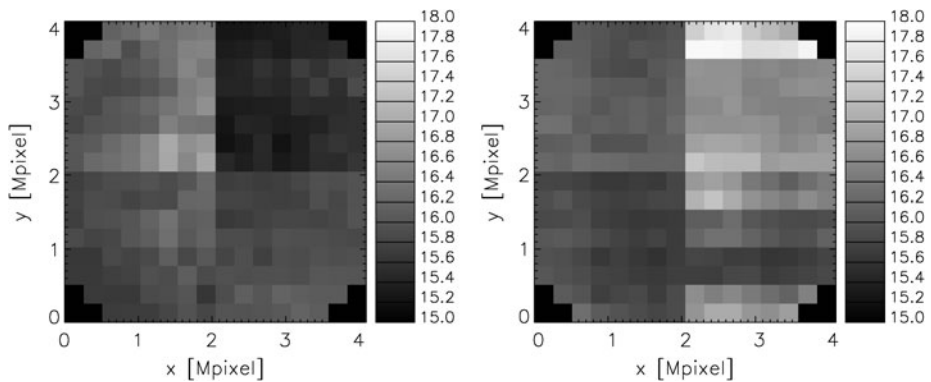


Figure 18 Inverse gain as a function of field position. The gray scale ranges from 15 through 18. The main signal comes from the four different amplifiers; the rest is due to inhomogeneities in the CCD.

Table 3 The inverse gain for the front and side cameras obtained from a variation in exposure.

	Front camera	Side camera
Lower left	15.91	15.83
Lower right	15.91	16.27
Upper left	16.27	16.10
Upper right	15.45	16.92

in a 64×64 rebinned imaged were fitted to a linear function of the exposure time (over the linear range) and the residuals plotted *versus* the intensity.

As can be seen from Figure 19, the intensities saturate at around 12 000 DN for both cameras. At intensities below that value, the nonlinearity is of the order 1%. The nonlinearity is generally very repeatable, but does show a weak temperature dependence.

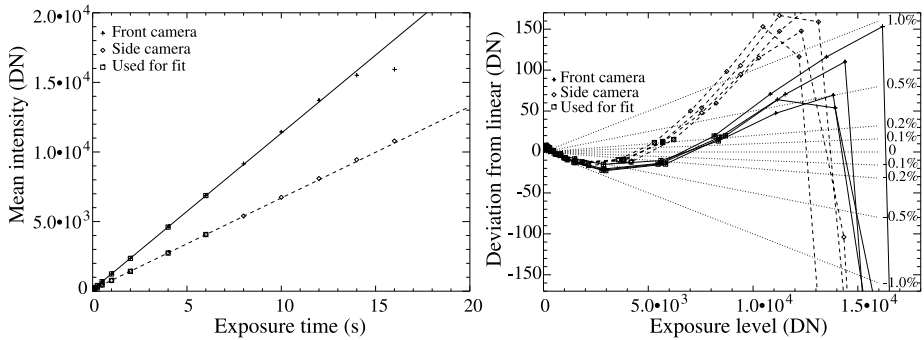


Figure 19 Left panel: Intensity as a function of exposure time for the front and side cameras. Only exposure times far away from the saturation level are used for the linear fit. Right panel: Residuals from a linear fit of the CCD intensity to the exposure time *versus* intensity. The four curves for each camera show the results for the four pixels closest to the center of the CCD in 64×64 rebinned images (*i.e.*, one per quadrant). All fits are done over the same set of exposure times.

11. Combining the Cameras

Depending on the choice of frame list (Couvidat *et al.*, 2011), it may be required to combine filtergrams from both cameras to produce a single observable. To avoid systematic errors from the procedures, an accurate knowledge and a high degree of stability for the shifts between the two cameras is required. Moreover, we need to know the flat fields of both cameras and their MTF.

The alignment of the cameras and their relative distortion can be measured by cross-correlating images. We measured the relative distortion and alignment with the random-dot target and fitted a fourth-order polynomial to fit the relative distortion. Doing so, we obtained a residual distortion with a magnitude of a few hundredths of a pixel, which reflects the structure of the CCD (see Figure 15, left panel). The obvious cause for this pattern is small inhomogeneities in the lattice of the CCD pixels. This structure is stable and can be modeled if necessary. Residual errors have a random, time-varying structure and are probably introduced by thermal fluctuations. They are of the order of a few hundredths of a pixel.

While the accuracy of the large-scale flat field that we obtain from the offpointing method for each individual camera is not sufficient to combine the cameras, we can very accurately determine the relative flat field from any image that is nearly simultaneously recorded in both cameras. The ratio of those images readily provides the relative flat field.

As shown in Section 3, we could not reliably measure any significant difference between the best focus MTF of both cameras on the ground. However, we know that the best focus of the cameras differs by 0.2 focus step, which leads to small differences in the MTF. As the main cause of uncertainty is the air currents, we may be able to find differences in the relative MTF and correct for them once we get data from space.

12. Conclusion

The *Helioseismic and Magnetic Imager* is a high-precision, near-monochromatic optical imager. The on-ground optical calibration shows that HMI meets all performance requirements and guarantees our ability to produce observables of sufficient quality to reach the HMI science goals. It also gives a clear guideline for the in-orbit calibration.

HMI is expected to achieve a Strehl ratio of 0.8 or better. The distortion of up to two pixels at the edge of the field of view has been determined with an accuracy of 0.05 pixel. The large-scale flat field can be determined with an accuracy of 0.2%, and for the small-scale flat field we confirmed that knowing the flat field in-flight at any time with an accuracy of 0.1% or better is realistic. The instrument focus varies from center to edge by 0.4 mm, and from edge to edge by less than 0.5 mm. The best focus is in the middle of the adjustable focus range, and the offset and rotation of the two cameras have been determined to fractions of a pixel.

Modeling helped us to understand the behavior of the instrument in a sometimes unstable temperature environment and also helped us ensure that the instrument will meet the specifications when operated in space. Continuous monitoring of the instrument's performance during a time period of more than two years has made us confident that HMI will provide data of outstanding quality during its mission.

Acknowledgements This work has been supported by the NASA grant NAS5-02139 (HMI). Many people were involved in the calibration efforts for the instrument. We thank staff members at LMATC, GSFC, and ASO for their support. In particular, we thank Dave Kirkpatrick, Darrel Torgerson, Bob Stern, and Brett Allard. We also thank Phil Scherrer, Ted Tarbell, and Alan Title for their input.

Open Access This article is distributed under the terms of the Creative Commons Attribution Noncommercial License which permits any noncommercial use, distribution, and reproduction in any medium, provided the original author(s) and source are credited.

References

- Bray, R.J., Loughhead, R.E.: 1979, *Sunspots*, Dover, New York.
- Couvidat, S., Zhao, J., Birch, A.C., Kosovichev, A.G., Duvall, T.L., Parchevsky, K., Scherrer, P.H.: 2010, Implementation and comparison of acoustic travel-time measurement procedures for the solar dynamics observatory/helio-seismic and magnetic imager time-distance helioseismology pipeline. *Solar Phys.* doi:[10.1007/s11207-010-9652-y](https://doi.org/10.1007/s11207-010-9652-y).
- Couvidat, S., Schou, J., Shine, R.A., Scherrer, P.H., Bush, R.I.: 2011, Wavelength dependence of the helioseismic and magnetic imager instrument. *Solar Phys.*, submitted.
- Jefferies, S.M., Duvall, T.L. Jr.: 1991, A simple method for correcting spatially resolved solar intensity oscillation observations for variations in scattered light. *Solar Phys.* **132**, 215–222. doi:[10.1007/BF00152283](https://doi.org/10.1007/BF00152283).
- Korzennik, S.G., Rabello-Soares, M.C., Schou, J.: 2004, On the determination of Michelson Doppler imager high-degree mode frequencies. *Astrophys. J.* **602**, 481–516. doi:[10.1086/381021](https://doi.org/10.1086/381021).
- Kuhn, J.R., Lin, H., Loran, D.: 1991, Gain calibrating nonuniform image-array data using only the image data. *Publ. Astron. Soc. Pac.* **103**, 1097–1108.
- Pierce, A.K., Slaughter, C.D.: 1977, Solar limb darkening. I – At wavelengths of 3033–7297. *Solar Phys.* **51**, 25–41. doi:[10.1007/BF00240442](https://doi.org/10.1007/BF00240442).
- Schou, J., Scherrer, P.H., Bush, R.I., Wachter, R., Couvidat, S., Rabello-Soares, M.C., Liu, Y., Hoeksema, J.T., Bogart, R.S., Duvall, J.T.L., Miles, J.W., Title, A.M., Shine, R.A., Tarbell, T.D., Allard, B.A., Wolfson, C.J., Tomczyk, S., Norton, A.A., Elmore, D.F., Borrero, J.M.: 2011, The helioseismic and magnetic imager instrument design and calibration. *Solar Phys.*, in preparation.
- Toner, C.G., Jefferies, S.M., Duvall, T.L. Jr.: 1997, Restoration of long-exposure full-disk solar intensity images. *Astrophys. J.* **478**, 817–827. doi:[10.1086/303836](https://doi.org/10.1086/303836).
- Toussaint, R.M., Harvey, J.W., Toussaint, D.: 2003, Improved convergence for CCD gain calibration using simultaneous-overrelaxation techniques. *Astron. J.* **126**, 1112–1118. doi:[10.1086/376846](https://doi.org/10.1086/376846).
- Wachter, R., Schou, J.: 2009, Inferring small-scale flatfields from solar rotation. *Solar Phys.* **258**, 331–341. doi:[10.1007/s11207-009-9406-x](https://doi.org/10.1007/s11207-009-9406-x).